



Supplementary Materials for

Extreme ultraviolet metalens by vacuum guiding

Marcus Ossiander *et al.*

Corresponding authors: Marcus Ossiander, mossiander@g.harvard.edu; Federico Capasso, capasso@seas.harvard.edu;
Martin Schultze, schultze@tugraz.at

Science **380**, 59 (2023)
DOI: 10.1126/science.adg6881

The PDF file includes:

Materials and Methods
Figs. S1 to S6
References

Materials and Methods

1 Rigorous coupled wave analysis and finite-difference time-domain simulations

We use refractive index data for extreme ultraviolet radiation (EUV) distributed with the IMD software package (21). For this project, specifically, we used crystalline Silicon data reported by Edwards, Palik, and Ghosh (22). To obtain metaatom libraries, we calculate the hole-diameter dependent transmission phases for different square unit cell sizes using rigorous coupled-wave analysis (S4 (42)). To model full-device performance, we simulate a Gaussian beam incident on the perforated silicon membrane and a three-wavelength-thick vacuum spacer region before and after the membrane using finite-difference time-domain modeling (Ansys Lumerical FDTD). In this region, all near-fields decay, thus, we model the subsequent evolution using Rayleigh-Sommerfeld diffraction.

2 Fabrication

To allow fabrication of our metasurface, we require a minimum hole diameter of 20 nm and at least 40 nm distance between neighboring holes to retain membrane stability. To increase the stability of our membrane further, we omit holes in our design on a 1 μm thick scaffolding grid spaced by 10 \times 10 μm (see Fig. 2F). The omission of holes does not limit the achievable focal spot but slightly decreases the efficiency (27). The fabrication of holes with accurate sub-100 nm diameter is challenging, therefore, we separate all holes into six groups using their diameter (20-30 nm, 30-40 nm, 40-50 nm, 50-60 nm, 60-70 nm, 70-80 nm) and use a different exposure dose and fabrication offset (i.e., the diameter we write during lithography is different than the diameter of the final etched hole) for each group.

The fabrication process is illustrated in Fig. S3: we start with a silicon-on-insulator wafer with a 220 nm thick silicon device layer, 3 μm thick buried oxide layer, and 725 μm thick silicon carrier layer. We deposit a silica hard mask layer using plasma-enhanced chemical vapor deposition (Surface Technology Systems). We then spin-coat a positive tone resist (MicroChemicals GmbH, AZ 4620) and expose marker structures using a maskless aligner (Heidelberg Instruments Mikrotechnik GmbH, MLA150). After development (MicroChemicals GmbH, AZ 400K) we etch the marker structures through the entire wafer (SPTS Technologies, Omega LPX Rapier) using reactive ion etching. In the following, we use the markers to align front and back side structures. We then spin-coat a layer of positive electron beam lithography resist (Zeon Corporation, ZEP520A). We then expose the metalens pattern using electron-beam lithography (Elionix, HS-50) and develop (o-Xylene). Subsequently, we transfer the metalens pattern first to the silica hard mask layer using inductively coupled plasma reactive ion etching (Surface Technology Systems, ICP RIE) and then to the silicon device layer using non-Bosch reactive ion etching (SPTS Technologies, Omega LPX Rapier). We then remove the silica hard mask layer using buffered Hydrofluoric acid. After defining the metalens pattern, we define the membrane area on the backside of the wafer using a spin-coated positive photoresist layer (MicroChemicals GmbH, AZ 4620) and a maskless aligner (Heidelberg Instruments Mikrotechnik GmbH, MLA150). After exposure and development (MicroChemicals GmbH, AZ 400K), we etch away the silicon carrier layer (SPTS Technologies, Omega LPX Rapier). To protect the thin membrane, we stop as soon as we can see the metasurface. This can leave behind a few microns of carrier silicon (less than 1 % of the initial thickness) at the bottom edges of the hole. We then remove the buried oxide layer by dripping hydrofluoric acid on the sample. Again, we stop the

process as soon as the metasurface is uncovered. The non-uniform black pattern in Fig. S4 is remaining silicon at the bottom edges of the hole with the bubble-shaped edges caused by the wet etch. As long as the entire metasurface is uncovered, we do not further remove it. The hydrofluoric acid wet etch also minimizes the formation of a silicon native oxide which strongly absorbs EUV (43).

The presented concept and simulations can be transferred directly to shorter wavelengths. However, as other materials must be used (e.g., for 13.5 nm wavelength, palladium, rhenium, or ruthenium), the fabrication recipe must be adapted. The electron beam lithography step is challenging for the feature pitches and sizes required at 13.5 nm wavelength but within the manufacturer specifications of available tools. As shorter wavelengths require less material thickness for a 2π phase shift, the required holes' aspect ratios are similar and thus the etch process remains achievable. If the membrane thickness gets too thin to support itself, an unpatterned support can be added (e.g., a thin silicon membrane at 13.5 nm wavelength).

3 Laser System, high-harmonic-generation, and measurement setup.

We start with femtosecond pulses (1 mJ energy, 6 kHz repetition rate, 161 fs full-width-at-half-maximum pulse duration, 1030 nm wavelength) from an ytterbium-based and diode-pumped laser (Light Conversion, UAB, Pharos). In a high-vacuum environment, we focus these laser pulses ($f = 25$ cm) into an invar tube filled with argon gas to create an EUV attosecond pulse train via HHG. We adjust the argon pressure to achieve phase matching between the fundamental driving pulses and radiation generated at 25 eV photon energy (approx. 10 mbar argon pressure). The final HHG radiation contains spectral components from the fundamental photon energy to above 40 eV. We then route the generated radiation to the metasurface using an uncoated gold mirror (Thorlabs, Inc.) and filter spectral components below 20 eV photon energy using a 0.5 um thick aluminum foil (Lebow Co.). After the metasurface, we perform a knife-edge scan using a razor blade mounted on a piezo nanopositioner (Piezosystem Jena GmbH). We then disperse the transmitted radiation spectrally using a toroidal grating (450 lines per mm, 153 mm focal length, 8 mm usable aperture, Horiba, Ltd., 541 00 200) and detect radiation using a back-thinned charge-coupled-device camera (Greateyes GmbH, GE 1024 256 BI UV1) protected by an additional 0.5 um thick aluminum foil.

4 Efficiency determination

To evaluate the efficiency of the EUV metalens, we compare the incoming photon flux in the region of the metasurface Φ^{incoming} (area marked by the blue dashed circle in Fig. S5), the entire photon flux transmitted through the sample $\Phi^{\text{transmitted}}$, and the photon flux change $\Delta\Phi^{\text{knife edge}}$ recorded in the knife edge scan with the knife retracted and blocking the focus (see Fig. S5C). To determine the fraction of light not influenced by the metasurface we subtract the detected focused light $\Delta\Phi^{\text{knife edge}}$ from the entire photon flux transmitted through the sample $\Phi^{\text{transmitted}}$. Because the inserted razorblade only covers 0.6% more of the metasurface area than the retracted razorblade, we neglect its influence on the detected background field. Light lost to grating effects is diffracted to large angles and is never detected and not included in the overall transmission, the background field, or the focused intensity.

Furthermore, because the numerical aperture of the imaging grating is smaller than that of our metasurface, some light that is focused by the metalens is not detected. To estimate the collection efficiency, we use the measured beam profile (Fig. S5) and project it into the grating plane along the propagation direction using the focal distance of the metalens, the distance between

the metalens and the grating, and the effective free aperture of the grazing incidence imaging grating. We find that $\approx 14\%$ of the focused radiation is collected by the imaging grating and correct $\Delta\Phi^{\text{knife edge}}$ to obtain Φ^{focused} . We find the ratios

$$\frac{\phi^{\text{transmitted}}}{\phi^{\text{incoming}}} = 11\%, \frac{\phi^{\text{focused}}}{\phi^{\text{transmitted}}} = 48\%, \text{ and } \frac{\phi^{\text{focused}}}{\phi^{\text{incoming}}} = 5.5\%.$$

The theoretically predicted average metaatom transmission (see purple crosses in Fig. 2B) is 40 %. As discussed in the main manuscript (see Simulation of Nyquist-limited focusing), with the current unit cell configuration, we expect to lose about 53 % of the transmitted power to low-order diffraction, yielding $\left(\frac{\phi^{\text{transmitted}}}{\phi^{\text{incoming}}}\right)^{\text{theory}} = 19\%$. If we furthermore include 25% absorption in a 2 nm thick native silicon oxide, we expect $\left(\frac{\phi^{\text{transmitted}}}{\phi^{\text{incoming}}}\right)^{\text{theory, 2 nm oxide}} = 14\%$, comparable to the observed $\frac{\phi^{\text{transmitted}}}{\phi^{\text{incoming}}} = 11\%$.

To estimate the wavefront accuracy of the metalens from the focusing efficiency, we solve the Rayleigh Sommerfeld diffraction integral (34) for an incoming Gaussian beam focused by the phase profile of a diffraction-limited lens. This phase profile is modified by wavefront errors caused by a) the areas where holes are omitted to mechanically stabilize the metasurface (compare with Fig. 2F), b) the phase coverage being limited to 1.5π , and c) fabrication accuracy. 48 % focusing efficiency is caused by a root mean squared (RMS) wavefront error of $\lambda_{\text{vac}}/7.3$ ($\lambda_{\text{vac}} = 49.0$ nm). The omitted-hole areas alone cause an RMS wavefront error of $\lambda_{\text{vac}}/11.0$. The limited phase coverage alone causes an RMS wavefront error of $\lambda_{\text{vac}}/27.9$. Together, both yield an RMS wavefront error of $\lambda_{\text{vac}}/10.3$. Therefore, to explain the recorded focusing efficiency, we calculate an RMS wavefront error due to fabrication accuracy of $\lambda_{\text{vac}}/10.0$.

5 Focusing over an extended bandwidth.

The metalens also focuses light away from the design wavelength. Solving equation (1) for f yields:

$$f = \frac{\lambda_{\text{vac}} \varphi}{4\pi} - \frac{r^2\pi}{\varphi\lambda_{\text{vac}}} \approx -\frac{r^2\pi}{\varphi\lambda_{\text{vac}}}.$$

For numerical apertures smaller than 0.2, the second term dominates, and we can approximate the hyperbolic phase profile with a quadratic phase profile with less than 1% error. The exact phase φ imparted by a hole changes with the wavelength. However, the positions within a metalens at which holes with the same diameters occur (i.e., the radial zones in which the phase increases from 0 to 2π) remain the same. Therefore, for off-design wavelengths λ_{vac} , the focal length $f(\lambda_{\text{vac}})$ will shift compared to the design wavelength $\lambda_{\text{vac}}^{\text{design}}$ and design focal length f^{design} according to:

$$f(\lambda_{\text{vac}}) \approx f^{\text{design}} \frac{\lambda_{\text{vac}}^{\text{design}}}{\lambda_{\text{vac}}}.$$

High bandwidth is often required by applications with time resolution. As a test, we choose 2 eV bandwidth (supporting pulse durations down to 0.9 fs). Fig. S6 presents the focus of the metalens examined in Fig. 4 of the manuscript for light with 24, 25, and 26 eV photon energy. We

observe a clean focus over the entire bandwidth, with a focal shift less than the Rayleigh range, suggesting metlenses are applicable to ultrashort light pulses.

However, for photon energies far away from the design energy, the phase coverage within a zone will start deviating significantly from 2π . A simulation for 30 eV photon energy in Fig. S6D shows the effects: the focusing efficiency drops, sidelobes around the focus appear, and grating effects worsen.

6 Optics for EUV and soft x-rays

Due to the strong absorption of all materials, most state-of-the-art EUV optics, e.g., spherical and toroidal mirrors, Kirkpatrick-Baez doublets, and polycapillary optics (44–50) rely on reflection. Acceptable reflectivities are often only achievable for light with grazing incidence, which demands bulky optics. Together with requirements for high-quality surfaces, low wavefront errors, and specialized metallic and multilayer coatings (51, 52), this limits achievable numerical apertures and aggravates cost. As transmissive optics, absorptive Fresnel zone plates (53) have been demonstrated. The lack of usable optics also led to the exploration and demonstration of EUV focusing via gas plumes of resonant atoms (54) and preconditioning driving radiation and subsequent nonlinear frequency upconversion (55). In the soft x-ray spectrum (photon wavelength range 0.1 nm - 10 nm, photon energy range 124 eV - 12 keV (16)), material limitations - especially absorption - are partially relieved, and focusing can be achieved using refractive kinoform lenses (56, 57), few-step phase zone plated (58) and photon sieves (59). Furthermore, reflective binary phase control was demonstrated but with many-wavelength large feature sizes (60–62).

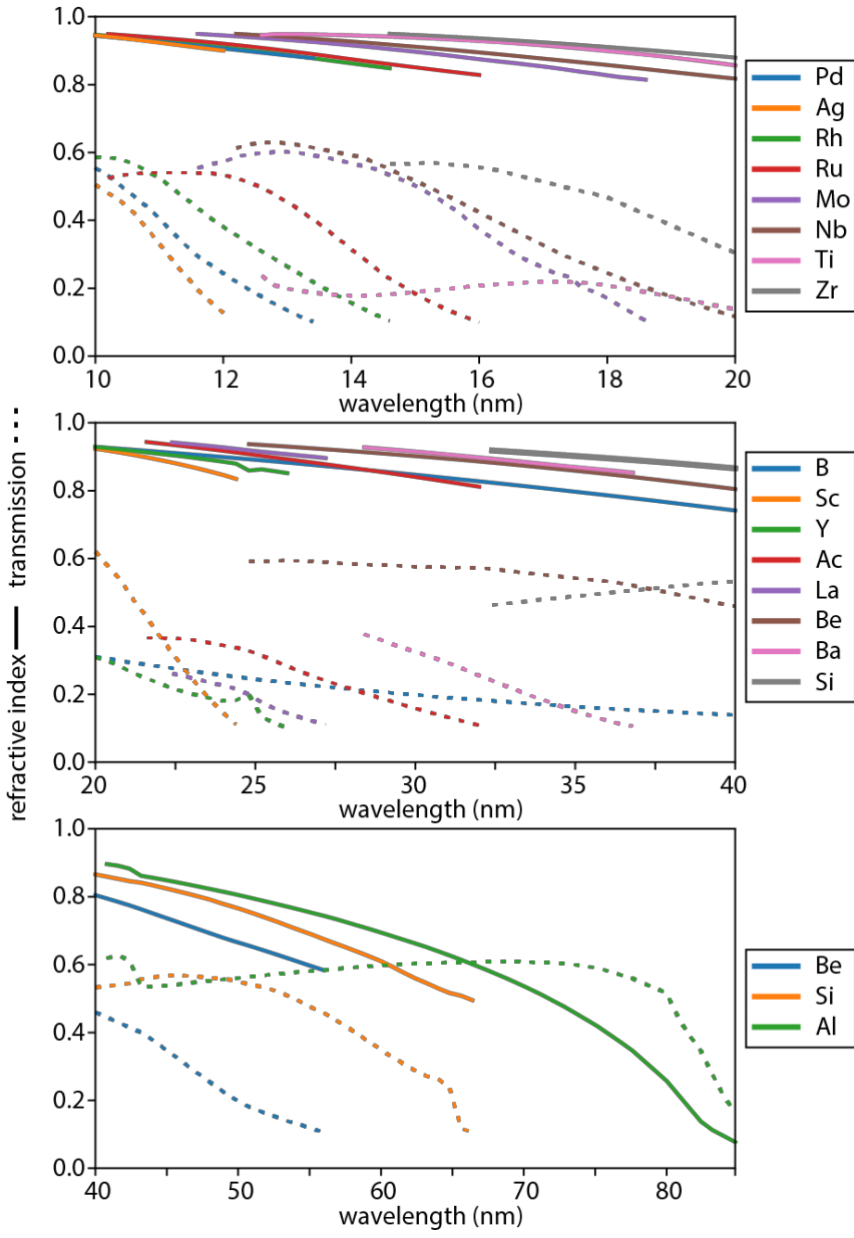


Fig. S1. Refractive indices of different materials in the EUV.

The wavelength-dependent real part of the refractive index is plotted as solid lines. Realizing a metasurface requires tuning the transmission phase within its limited thickness. The effective refractive index of a waveguide usually lies between the refractive index of the core (in this case vacuum, $n = 1$) and the cladding ($n < 1$). Therefore, the transmission of a solid layer of material with a thickness that induces a 2π propagation phase shift compared to propagation through the same thickness of vacuum yields a lower limit for the transmission of realizable metaatoms. We plot the transmission of layers of the respective materials at this 2π propagation phase thickness as dotted lines. Data is only displayed in spectral regions where the transmission at this 2π propagation phase thickness is larger than 10%. Data was taken from (21).

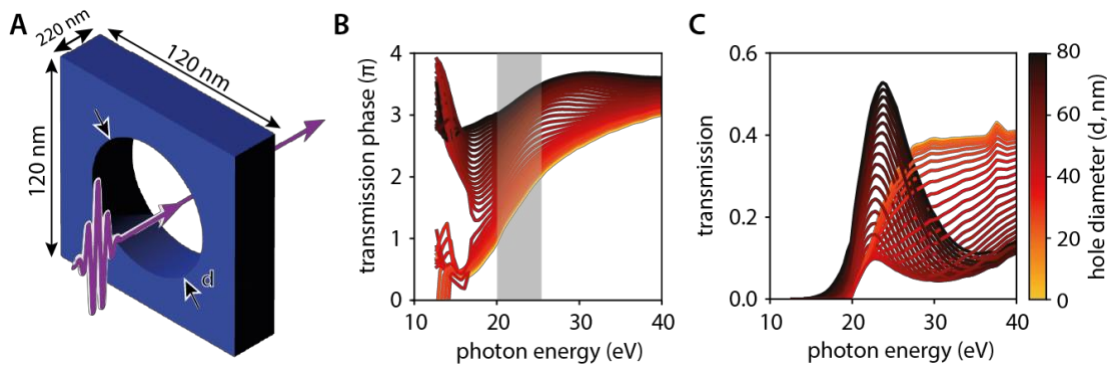


Fig. S2. Energy-dependent extreme ultraviolet transmission through a perforated membrane in the forward direction.

(A) simulation setup: we model the transmission of extreme ultraviolet light (purple arrow) passing through a 220 nm thick crystalline silicon membrane (blue) with a hole with diameter d . We model a single 120 nm x 120 nm unit cell with periodic boundary conditions.

(B) photon energy and hole diameter-dependent transmission phase (colored lines, see the color bar in panel (C)) of the 220 nm thick Silicon membrane with a hole. The grey area indicates the region where hole diameters from 20 nm to 80 nm offer phase coverage larger than 1.5π .

(C) photon energy and hole diameter-dependent intensity transmission into the zeroth diffraction order (colored lines) of the 220 nm thick silicon membrane with a hole.

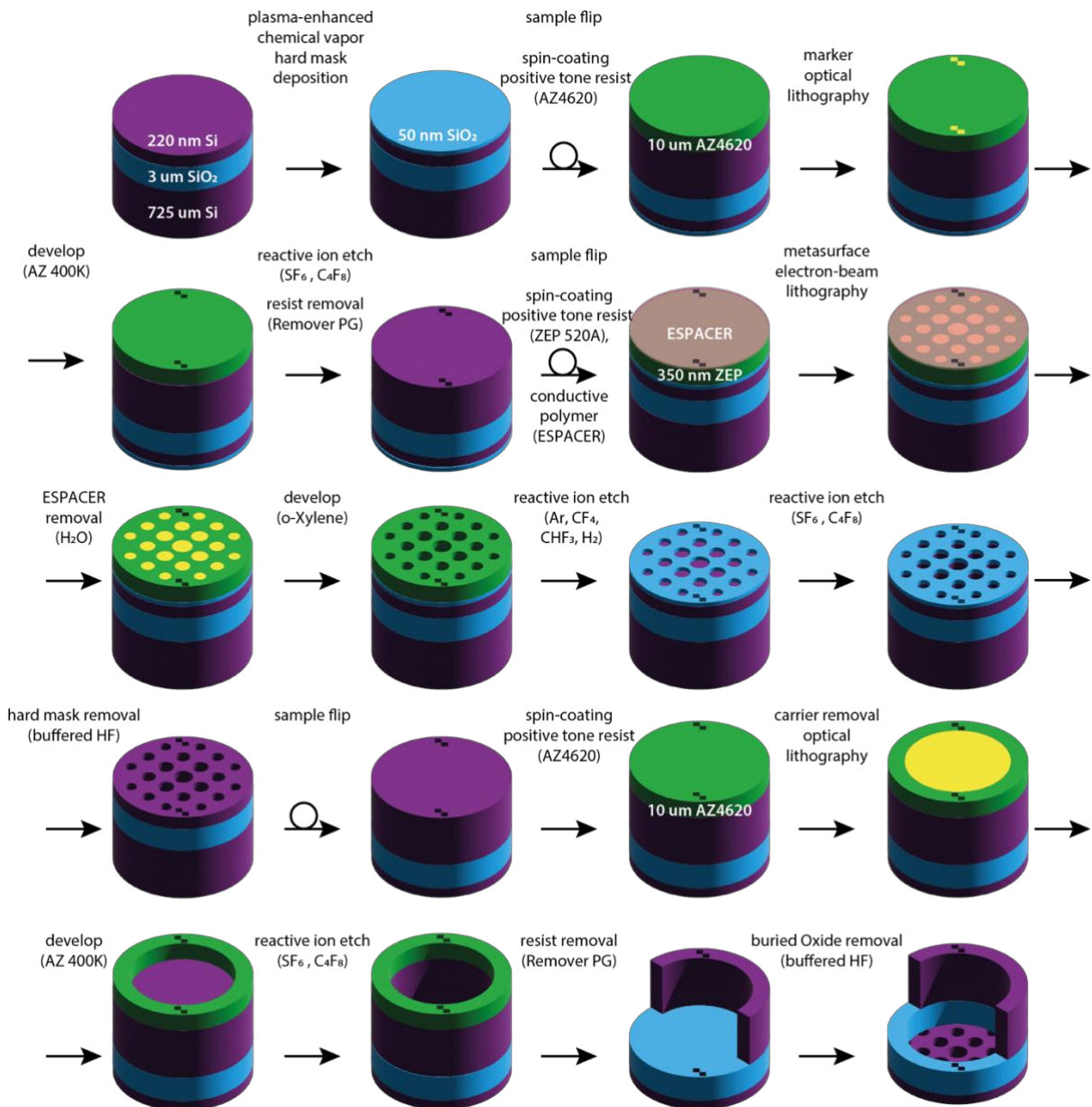


Fig. S3. Extreme ultraviolet metasurface fabrication (not to scale)

The base material is a silicon-on-insulator (SOI) wafer, consisting of a 220 nm device layer (silicon, purple), a 3 um buried oxide layer (silica, blue), and a 725 um carrier wafer (silicon, purple). A silica hard mask (blue) is deposited via chemical vapor deposition. The sample is spin-coated with a positive tone resist (green) and marker structures (yellow) are exposed using optical lithography. The exposed resist is removed using developer, and the entire wafer is etched away in these areas using reactive ion etching to create markers for aligning front and back side structures. Remaining resist is removed. Then, a positive tone electron beam lithography resist (green) and a conductive polymer (pink) are spin-coated. The metasurface pattern is written (yellow) using electron beam lithography, then the conductive polymer and the exposed resist are

removed using water and developer. The pattern is first etched through the hard mask and then through the device layer using reactive ion etching. The hard mask is removed using buffered Hydrofluoric acid. To create a free-standing membrane, positive tone resist is spin-coated on the back side of the sample (green), and the metasurface area is exposed using optical lithography (yellow). The exposed resist is removed using developer, and the Silicon carrier wafer is etched away in this area using reactive ion etching. Finally, the remaining resist is removed, and the buried oxide layer is etched away in the same area using buffered hydrofluoric acid.

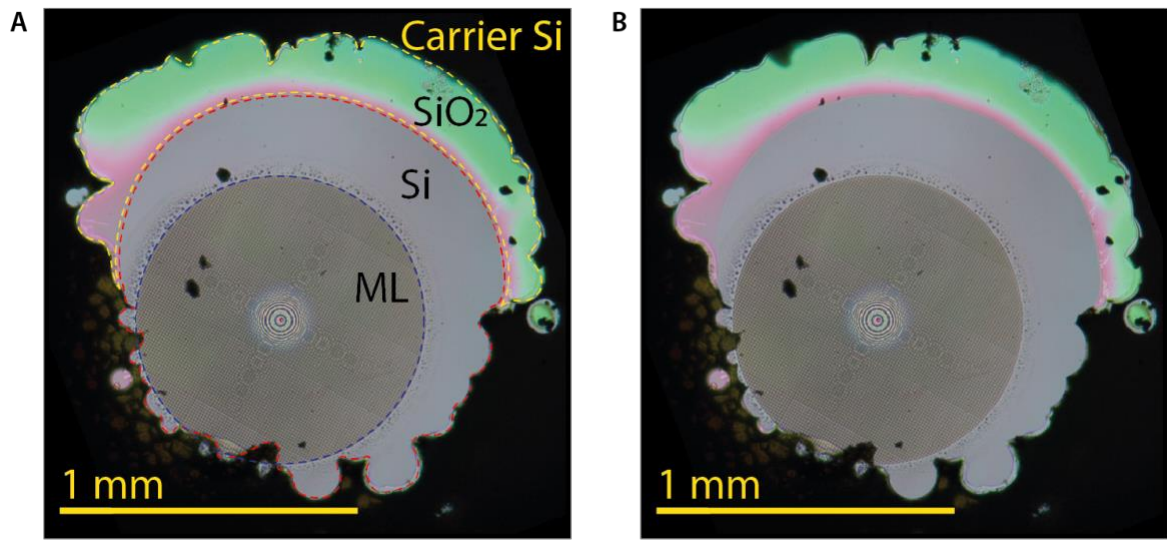


Fig. S4. Optical-microscope pictures of the final metalens membrane.

(A) With the overlay reproduced from Fig. 2G and Fig. 3B: the metasurface lens (ML) is encircled by the dashed blue line. Because the metalens features are too small to be resolved at this magnification, it shows a moiré pattern (ring patterns and bright area at the center). The unpatterned silicon membrane area appears solid grey (encircled by the dashed red line). Areas with remaining buried oxide layer appear red and green due to thin-film interference (encircled by the dashed yellow line). The silicon carrier wafer appears black.

(B) The same picture without the overlay.

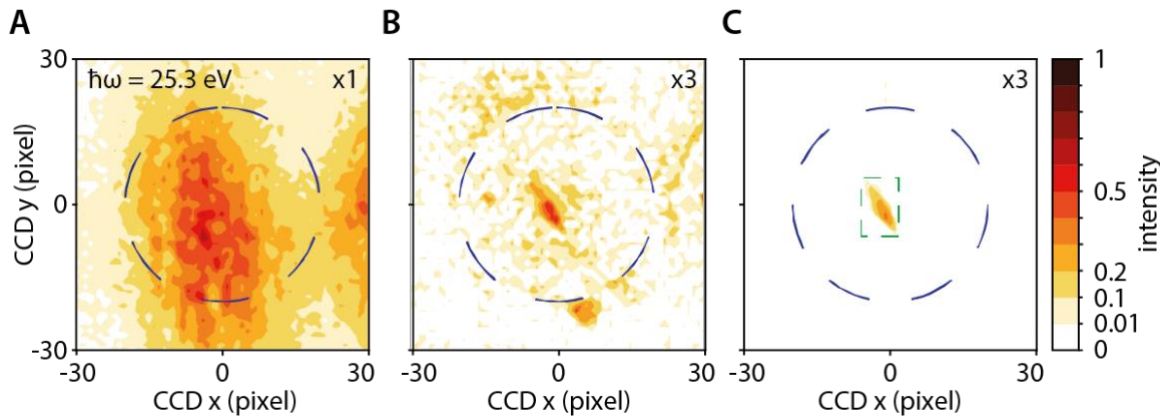


Fig. S5. Real space images of the experimental metasurface focal plane.

(A) incoming extreme ultraviolet beam profile (false color plot) at 25.3 eV photon energy (21st harmonic of the driving laser at 1030 nm wavelength) detected by the CCD. The dashed blue line marks the circumference of the metasurface (not inserted into the beam in this panel). Color bar in panel (C).

(B) extreme ultraviolet beam profile after the metasurface (false color plot) at 25.3 eV photon energy detected by the CCD. The dashed blue line marks the circumference of the metasurface. Color bar in panel (C), the photon flux was multiplied by a factor of 3 when compared with panel (A). This does not mean the focused intensity is smaller than the incoming beam intensity: because the imaging grating has a smaller numerical aperture than the metasurface, only 14 % of the focused light is collected. Furthermore, aberrations caused by using a grazing incidence toroidal imaging grating enlarge the observed focus compared to the real focus. The focal spot size measured using the knife-edge scan is considerably smaller than a single pixel of our CCD camera and yields an intensity enhancement in the focus of more than 27000.

(C) extreme ultraviolet fraction detected by the CCD that was focused by the metasurface (false color plot). We isolate focused radiation by subtracting a picture taken with the razor blade obstructing the focus from a picture without the razor blade blocking the focus. The dashed blue line marks the circumference of the metasurface. The dashed green line marks the light focused by the metasurface. The photon flux was multiplied by a factor of 3 when compared with panel (A).

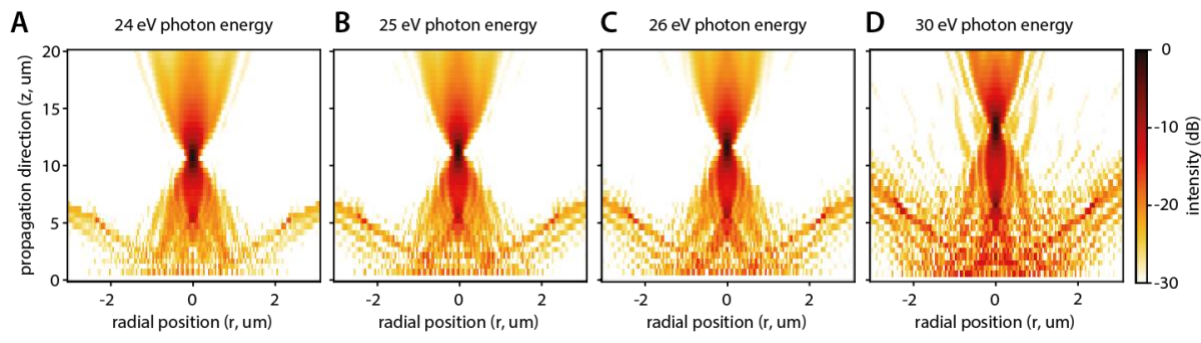


Fig. S6. Focusing over an extended bandwidth.

- (A) modeled light intensity evolution (false color plot) after the metasurface pictured in Fig. 4B focuses light with 24 eV photon energy. Color bar in panel (D).
- (B) same as (A) for 25 eV photon energy.
- (C) same as (A) for 26 eV photon energy.
- (D) same as (A) for 30 eV photon energy.

References and Notes

1. S. M. Kamali, E. Arbabi, A. Arbabi, A. Faraon, A review of dielectric optical metasurfaces for wavefront control. *Nanophotonics* **7**, 1041–1068 (2018). [doi:10.1515/nanoph-2017-0129](https://doi.org/10.1515/nanoph-2017-0129)
2. N. Yu, P. Genevet, M. A. Kats, F. Aieta, J.-P. Tetienne, F. Capasso, Z. Gaburro, Light propagation with phase discontinuities: Generalized laws of reflection and refraction. *Science* **334**, 333–337 (2011). [doi:10.1126/science.1210713](https://doi.org/10.1126/science.1210713) [Medline](#)
3. M. Khorasaninejad, W. T. Chen, R. C. Devlin, J. Oh, A. Y. Zhu, F. Capasso, Metalenses at visible wavelengths: Diffraction-limited focusing and subwavelength resolution imaging. *Science* **352**, 1190–1194 (2016). [doi:10.1126/science.aaf6644](https://doi.org/10.1126/science.aaf6644) [Medline](#)
4. N. Mahmood, I. Kim, M. Q. Mehmood, H. Jeong, A. Akbar, D. Lee, M. Saleem, M. Zubair, M. S. Anwar, F. A. Tahir, J. Rho, Polarisation insensitive multifunctional metasurfaces based on all-dielectric nanowaveguides. *Nanoscale* **10**, 18323–18330 (2018). [doi:10.1039/C8NR05633A](https://doi.org/10.1039/C8NR05633A) [Medline](#)
5. C. Spägle, M. Tamagnone, D. Kazakov, M. Ossiander, M. Piccardo, F. Capasso, Multifunctional wide-angle optics and lasing based on supercell metasurfaces. *Nat. Commun.* **12**, 3787 (2021). [doi:10.1038/s41467-021-24071-2](https://doi.org/10.1038/s41467-021-24071-2) [Medline](#)
6. R. C. Devlin, A. Ambrosio, N. A. Rubin, J. P. B. Mueller, F. Capasso, Arbitrary spin-to-orbital angular momentum conversion of light. *Science* **358**, 896–901 (2017). [doi:10.1126/science.aoa5392](https://doi.org/10.1126/science.aoa5392) [Medline](#)
7. N. A. Rubin, G. D’Aversa, P. Chevalier, Z. Shi, W. T. Chen, F. Capasso, Matrix Fourier optics enables a compact full-Stokes polarization camera. *Science* **365**, eaax1839 (2019). [doi:10.1126/science.aax1839](https://doi.org/10.1126/science.aax1839) [Medline](#)
8. Y. Intaravanne, X. Chen, Recent advances in optical metasurfaces for polarization detection and engineered polarization profiles. *Nanophotonics* **9**, 1003–1014 (2020). [doi:10.1515/nanoph-2019-0479](https://doi.org/10.1515/nanoph-2019-0479)
9. Y. Deng, X. Wang, Z. Gong, K. Dong, S. Lou, N. Pégard, K. B. Tom, F. Yang, Z. You, L. Waller, J. Yao, All-silicon broadband ultraviolet metasurfaces. *Adv. Mater.* **30**, e1802632 (2018). [doi:10.1002/adma.201802632](https://doi.org/10.1002/adma.201802632) [Medline](#)
10. K. Huang, J. Deng, H. S. Leong, S. L. K. Yap, R. B. Yang, J. Teng, H. Liu, Ultraviolet metasurfaces of $\approx 80\%$ efficiency with antiferromagnetic resonances for optical vectorial anti-counterfeiting. *Laser Photonics Rev.* **13**, 1800289 (2019). [doi:10.1002/lpor.201800289](https://doi.org/10.1002/lpor.201800289)
11. C. Zhang, S. Divitt, Q. Fan, W. Zhu, A. Agrawal, Y. Lu, T. Xu, H. J. Lezec, Low-loss metasurface optics down to the deep ultraviolet region. *Light Sci. Appl.* **9**, 55 (2020). [doi:10.1038/s41377-020-0287-y](https://doi.org/10.1038/s41377-020-0287-y) [Medline](#)
12. H. Liu, C. Guo, G. Vampa, J. L. Zhang, T. Sarmiento, M. Xiao, P. H. Bucksbaum, J. Vučković, S. Fan, D. A. Reis, Enhanced high-harmonic generation from an all-dielectric metasurface. *Nat. Phys.* **14**, 1006–1010 (2018). [doi:10.1038/s41567-018-0233-6](https://doi.org/10.1038/s41567-018-0233-6)
13. A. Ahmadvand, M. Semmlinger, L. Dong, B. Gerislioglu, P. Nordlander, N. J. Halas, Toroidal dipole-enhanced third harmonic generation of deep ultraviolet light using

plasmonic meta-atoms. *Nano Lett.* **19**, 605–611 (2019). [doi:10.1021/acs.nanolett.8b04798](https://doi.org/10.1021/acs.nanolett.8b04798) [Medline](#)

14. M. Semmlinger, M. Zhang, M. L. Tseng, T.-T. Huang, J. Yang, D. P. Tsai, P. Nordlander, N. J. Halas, Generating third harmonic vacuum ultraviolet light with a TiO₂ metasurface. *Nano Lett.* **19**, 8972–8978 (2019). [doi:10.1021/acs.nanolett.9b03961](https://doi.org/10.1021/acs.nanolett.9b03961) [Medline](#)
15. M. L. Tseng, M. Semmlinger, M. Zhang, C. Arndt, T.-T. Huang, J. Yang, H. Y. Kuo, V.-C. Su, M. K. Chen, C. H. Chu, B. Cerjan, D. P. Tsai, P. Nordlander, N. J. Halas, Vacuum ultraviolet nonlinear metalens. *Sci. Adv.* **8**, eabn5644 (2022). [doi:10.1126/sciadv.abn5644](https://doi.org/10.1126/sciadv.abn5644) [Medline](#)
16. W. K. Tobiska, A. Nusinov, “Status of ISO draft international standard for determining solar irradiances (Dros. Inf. Serv. 21348)” in *35th COSPAR Scientific Assembly* (Committee on Space Research, 2004), pp. 1–10.
17. F. Krausz, M. Ivanov, Attosecond physics. *Rev. Mod. Phys.* **81**, 163–234 (2009). [doi:10.1103/RevModPhys.81.163](https://doi.org/10.1103/RevModPhys.81.163)
18. B. Turkot, S. Carson, A. Lio, “Continuing Moore’s law with EUV lithography” in *2017 IEEE International Electron Devices Meeting (IEDM)* (IEEE, 2017), pp. 14.4.1–14.4.3.
19. Materials and methods are available as supplementary materials.
20. A. Thompson, D. Attwood, E. Gullikson, M. Howells, J. E. Kim, J. Kirz, J. Kortright, I. Lindsay, Y. Liu, P. Pianetta, A. Robinson, J. Scofield, J. Underwood, G. Williams, H. Winick, “X-ray data booklet” (LBNL/PUB 490 Rev. 3, Lawrence Berkeley National Laboratory, 2009).
21. D. L. Windt, IMD—Software for modeling the optical properties of multilayer films. *Comput. Phys.* **12**, 360–370 (1998). [doi:10.1063/1.168689](https://doi.org/10.1063/1.168689)
22. E. D. Palik, G. Ghosh, Eds., *Handbook of Optical Constants of Solids* (Academic Press, 1998).
23. S. W. D. Lim, M. L. Meretska, F. Capasso, A high aspect ratio inverse-designed holey metalens. *Nano Lett.* **21**, 8642–8649 (2021). [doi:10.1021/acs.nanolett.1c02612](https://doi.org/10.1021/acs.nanolett.1c02612) [Medline](#)
24. M. Hentschel, K. Koshelev, F. Sterl, S. Both, J. Karst, L. Shamsafar, T. Weiss, Y. Kivshar, H. Giessen, Dielectric Mie voids: Confining light in air. *Light Sci. Appl.* **12**, 3 (2023). [doi:10.1038/s41377-022-01015-z](https://doi.org/10.1038/s41377-022-01015-z) [Medline](#)
25. C. M. Smith, N. Venkataraman, M. T. Gallagher, D. Müller, J. A. West, N. F. Borrelli, D. C. Allan, K. W. Koch, Low-loss hollow-core silica/air photonic bandgap fibre. *Nature* **424**, 657–659 (2003). [doi:10.1038/nature01849](https://doi.org/10.1038/nature01849) [Medline](#)
26. T. W. Ebbesen, H. J. Lezec, H. F. Ghaemi, T. Thio, P. A. Wolff, Extraordinary optical transmission through sub-wavelength hole arrays. *Nature* **391**, 667–669 (1998). [doi:10.1038/35570](https://doi.org/10.1038/35570)
27. J.-S. Park, S. Zhang, A. She, W. T. Chen, P. Lin, K. M. A. Yousef, J.-X. Cheng, F. Capasso, All-glass, large metalens at visible wavelength using deep-ultraviolet projection lithography. *Nano Lett.* **19**, 8673–8682 (2019). [doi:10.1021/acs.nanolett.9b03333](https://doi.org/10.1021/acs.nanolett.9b03333) [Medline](#)

28. W. T. Chen, A. Y. Zhu, V. Sanjeev, M. Khorasaninejad, Z. Shi, E. Lee, F. Capasso, A broadband achromatic metalens for focusing and imaging in the visible. *Nat. Nanotechnol.* **13**, 220–226 (2018). [doi:10.1038/s41565-017-0034-6](https://doi.org/10.1038/s41565-017-0034-6) [Medline](#)
29. S. M. Kamali, E. Arbabi, A. Arbabi, Y. Horie, A. Faraon, Highly tunable elastic dielectric metasurface lenses. *Laser Photonics Rev.* **10**, 1002–1008 (2016). [doi:10.1002/lpor.201600144](https://doi.org/10.1002/lpor.201600144)
30. P. B. Corkum, Plasma perspective on strong field multiphoton ionization. *Phys. Rev. Lett.* **71**, 1994–1997 (1993). [doi:10.1103/PhysRevLett.71.1994](https://doi.org/10.1103/PhysRevLett.71.1994) [Medline](#)
31. M. Lewenstein, P. Balcou, M. Y. Ivanov, A. L’Huillier, P. B. Corkum, Theory of high-harmonic generation by low-frequency laser fields. *Phys. Rev. A* **49**, 2117–2132 (1994). [doi:10.1103/PhysRevA.49.2117](https://doi.org/10.1103/PhysRevA.49.2117) [Medline](#)
32. A. L’Huillier, K. J. Schafer, K. C. Kulander, Theoretical aspects of intense field harmonic generation. *J. Phys. At. Mol. Opt. Phys.* **24**, 3315–3341 (1991). [doi:10.1088/0953-4075/24/15/004](https://doi.org/10.1088/0953-4075/24/15/004)
33. A. H. Firester, M. E. Heller, P. Sheng, Knife-edge scanning measurements of subwavelength focused light beams. *Appl. Opt.* **16**, 1971–1974 (1977). [doi:10.1364/AO.16.001971](https://doi.org/10.1364/AO.16.001971) [Medline](#)
34. R. L. Lucke, “Rayleigh-Sommerfeld diffraction vs Fresnel-Kirchhoff, Fourier propagation, and Poisson’s spot” (NRL/FR/7218-04-10,001, Naval Research Laboratory, 2004).
35. B. E. A. Saleh, M. C. Teich, *Fundamentals of Photonics* (Wiley, 2007).
36. H.-S. Chon, G. Park, S.-B. Lee, S. Yoon, J. Kim, J.-H. Lee, K. An, Dependence of transverse and longitudinal resolutions on incident Gaussian beam widths in the illumination part of optical scanning microscopy. *J. Opt. Soc. Am. A Opt. Image Sci. Vis.* **24**, 60–67 (2007). [doi:10.1364/JOSAA.24.000060](https://doi.org/10.1364/JOSAA.24.000060) [Medline](#)
37. M. Ossiander, K. Golyari, K. Scharl, L. Lehnert, F. Siegrist, J. P. Bürger, D. Zimin, J. A. Gessner, M. Weidman, I. Floss, V. Smejkal, S. Donsa, C. Lemell, F. Libisch, N. Karpowicz, J. Burgdörfer, F. Krausz, M. Schultze, The speed limit of optoelectronics. *Nat. Commun.* **13**, 1620 (2022). [doi:10.1038/s41467-022-29252-1](https://doi.org/10.1038/s41467-022-29252-1) [Medline](#)
38. M. Rimmer, Analysis of perturbed lens systems. *Appl. Opt.* **9**, 533–537 (1970). [doi:10.1364/AO.9.000533](https://doi.org/10.1364/AO.9.000533) [Medline](#)
39. J. Zhu, S. Zhang, S. Xie, C. Xu, L. Zhang, X. Tao, Y. Ren, Y. Wang, B. Deng, R. Tai, Y. Chen, Nanofabrication of 50 nm zone plates through e-beam lithography with local proximity effect correction for x-ray imaging. *Chin. Phys. B* **29**, 047501 (2020). [doi:10.1088/1674-1056/ab7800](https://doi.org/10.1088/1674-1056/ab7800)
40. G. W. Webb, I. V. Minin, O. V. Minin, Variable reference phase in diffractive antennas: Review, applications, new results. *IEEE Antennas Propag. Mag.* **53**, 77–94 (2011). [doi:10.1109/MAP.2011.5949329](https://doi.org/10.1109/MAP.2011.5949329)
41. M. Ossiander, M. L. Meretska, H. K. Hampel, S. W. D. Lim, N. Knefz, T. Jauk, F. Capasso, M. Schultze, Data for “Extreme ultraviolet metalens by vacuum guiding.” figshare (2023); <https://doi.org/10.6084/m9.figshare.22191457>.

42. V. Liu, S. Fan, S⁴: A free electromagnetic solver for layered periodic structures. *Comput. Phys. Commun.* **183**, 2233–2244 (2012). [doi:10.1016/j.cpc.2012.04.026](https://doi.org/10.1016/j.cpc.2012.04.026)
43. T. Takahagi, I. Nagai, A. Ishitani, H. Kuroda, Y. Nagasawa, The formation of hydrogen passivated silicon single-crystal surfaces using ultraviolet cleaning and HF etching. *J. Appl. Phys.* **64**, 3516–3521 (1988). [doi:10.1063/1.341489](https://doi.org/10.1063/1.341489)
44. N. R. Böwering, A. I. Ershov, W. F. Marx, O. V. Khodykin, B. A. M. Hansson, E. Vargas L., J. A. Chavez, I. V. Fomenkov, D. W. Myers, D. C. Brandt, “EUV source collector” in *Proceedings of the SPIE 31st International Symposium on Advanced Lithography, vol. 6151, Emerging Lithographic Technologies X*, M. J. Lercel, Ed. (SPIE, 2006), p. 61513R.
45. B. Wu, A. Kumar, Extreme ultraviolet lithography: A review. *J. Vac. Sci. Technol. B Microelectron. Nanometer Struct. Process. Meas. Phenom.* **25**, 1743–1761 (2007). [doi:10.1116/1.2794048](https://doi.org/10.1116/1.2794048)
46. C. Bourassin-Bouchet, M. M. Mang, F. Delmotte, P. Chavel, S. de Rossi, How to focus an attosecond pulse. *Opt. Express* **21**, 2506–2520 (2013). [doi:10.1364/OE.21.002506](https://doi.org/10.1364/OE.21.002506) [Medline](#)
47. L. Poletto, F. Frassetto, F. Calegari, S. Anumula, A. Trabattoni, M. Nisoli, Micro-focusing of attosecond pulses by grazing-incidence toroidal mirrors. *Opt. Express* **21**, 13040–13051 (2013). [doi:10.1364/OE.21.013040](https://doi.org/10.1364/OE.21.013040) [Medline](#)
48. H. Coudert-Alteirac, H. Dacasa, F. Campi, E. Kueny, B. Farkas, F. Brunner, S. Maclot, B. Manschwetus, H. Wikmark, J. Lahl, L. Rading, J. Peschel, B. Major, K. Varjú, G. Dovillaire, P. Zeitoun, P. Johnsson, A. L’Huillier, P. Rudawski, Micro-focusing of broadband high-order harmonic radiation by a double toroidal mirror. *Appl. Sci.* **7**, 1159 (2017). [doi:10.3390/app7111159](https://doi.org/10.3390/app7111159)
49. P. P. Naulleau, K. A. Goldberg, P. J. Batson, S. Jeong, J. H. Underwood, Tolerancing of diffraction-limited Kirkpatrick-Baez synchrotron beamline optics for extreme-ultraviolet metrology. *Appl. Opt.* **40**, 3703–3709 (2001). [doi:10.1364/AO.40.003703](https://doi.org/10.1364/AO.40.003703) [Medline](#)
50. C. A. MacDonald, Focusing polycapillary optics and their applications. *X-Ray Opt. Instrum.* **2010**, 1–17 (2010). [doi:10.1155/2010/867049](https://doi.org/10.1155/2010/867049)
51. E. Spiller, Reflective multilayer coatings for the far UV region. *Appl. Opt.* **15**, 2333–2338 (1976). [doi:10.1364/AO.15.002333](https://doi.org/10.1364/AO.15.002333) [Medline](#)
52. A. Guggenmos, U. Kleineberg, “Multilayer mirrors for attosecond pulses” in *Advances in Optics: Reviews, Vol. 1*, S. Y. Yurish, Ed. (International Frequency Sensor Association Publishing, 2018).
53. W. Chao, J. Kim, S. Rekawa, P. Fischer, E. H. Anderson, Demonstration of 12 nm resolution Fresnel zone plate lens based soft x-ray microscopy. *Opt. Express* **17**, 17669–17677 (2009). [doi:10.1364/OE.17.017669](https://doi.org/10.1364/OE.17.017669) [Medline](#)
54. L. Drescher, O. Kornilov, T. Witting, G. Reitsma, N. Monserud, A. Rouzée, J. Mikosch, M. J. J. Vrakking, B. Schütte, Extreme-ultraviolet refractive optics. *Nature* **564**, 91–94 (2018). [doi:10.1038/s41586-018-0737-3](https://doi.org/10.1038/s41586-018-0737-3) [Medline](#)

55. L. Quintard, V. Strelkov, J. Vabek, O. Hort, A. Dubrouil, D. Descamps, F. Burgy, C. Péjot, E. Mével, F. Catoire, E. Constant, Optics-less focusing of XUV high-order harmonics. *Sci. Adv.* **5**, eaau7175 (2019). [doi:10.1126/sciadv.aau7175](https://doi.org/10.1126/sciadv.aau7175) [Medline](#)
56. K. Keskinbora, U. T. Sanli, C. Grévent, G. Schütz, “Fabrication and x-ray testing of true kinoform lenses with high efficiencies” in *Proceedings SPIE Optical Engineering and Applications*, vol. 9592, *X-Ray Nanoimaging: Instruments and Methods II*, B. Lai, Ed. (SPIE, 2015), p. 95920H.
57. U. T. Sanli, H. Ceylan, I. Bykova, M. Weigand, M. Sitti, G. Schütz, K. Keskinbora, K. Keskinbora, 3D nanoprinted plastic kinoform x-ray optics. *Adv. Mater.* **30**, 1802503 (2018). [doi:10.1002/adma.201802503](https://doi.org/10.1002/adma.201802503)
58. E. Di Fabrizio, F. Romanato, M. Gentili, S. Cabrini, B. Kaulich, J. Susini, R. Barrett, High-efficiency multilevel zone plates for keV x-rays. *Nature* **401**, 895–898 (1999). [doi:10.1038/44791](https://doi.org/10.1038/44791)
59. L. Kipp, M. Skibowski, R. L. Johnson, R. Berndt, R. Adelung, S. Harm, R. Seemann, Sharper images by focusing soft x-rays with photon sieves. *Nature* **414**, 184–188 (2001). [doi:10.1038/35102526](https://doi.org/10.1038/35102526) [Medline](#)
60. F. Salmassi, P. P. Naulleau, E. M. Gullikson, D. L. Olynick, J. A. Liddle, Extreme ultraviolet binary phase gratings: Fabrication and application to diffractive optics. *J. Vac. Sci. Technol. A* **24**, 1136–1140 (2006). [doi:10.1116/1.2212435](https://doi.org/10.1116/1.2212435)
61. P. P. Naulleau, F. Salmassi, E. M. Gullikson, E. H. Anderson, “Holographic optical elements for the extreme-ultraviolet regime” in *Proceedings SPIE MOEMS-MEMS 2007 Micro and Nanofabrication*, vol. 6462, *Micromachining Technology for Micro-Optics and Nano-Optics V and Microfabrication Process Technology XII*, M.-A. Maher, H. D. Stewart, J.-C. Chiao, T. J. Suleski, E. G. Johnson, G. P. Nordin, Eds. (SPIE, 2007), p. 64620S.
62. F. Döring, B. Rösner, M. Langer, A. Kubec, A. Kleibert, J. Raabe, C. A. F. Vaz, M. Lebugle, C. David, Multifocus off-axis zone plates for x-ray free-electron laser experiments. *Optica* **7**, 1007–1014 (2020). [doi:10.1364/OPTICA.398022](https://doi.org/10.1364/OPTICA.398022)